ACS APPLIED ELECTRONIC MATERIALS

pubs.acs.org/acsaelm Article

MXene-Molecular Chromophore Triboelectric Systems for Self-Powered Noble-Gas Discharge

Published as part of ACS Applied Electronic Materials special issue "2D MXenes at the Interface of Materials and Electronics".

Suman Mudu, Vijaykumar Chuncha, M. Navaneeth, Pembarthi Raju, Kamakshaiah Charyulu Devarayapalli, Raghu Chitta, Manjula G, Palash Mishra, Dae Sung Lee, Uday Kumar Khanapuram,* and Rakesh Kumar Rajaboina*

Cite This: https://doi.org/10.1021/acsaelm.5c02701 Read Online

ACCESS | Metrics & More | Article Recommendations | Supporting Information

ABSTRACT: Identifying triboelectric material pairs capable of delivering high performance remains a key challenge for advancing triboelectric nanogenerator (TENG) technologies. To address the challenge, we have investigated a triboelectric pair comprising tribo-negative PDMS/MXene($Ti_3C_2T_x$) with a potent tribo-positive material, triphenylamine−phenyl−benzothiazole (TPA-Ph-BTZ). In this work, the triboelectric propertiesof TPA-Ph-BTZ were first systematically determined by pairing it with a series of standard frictional materials, confirming that TPA-Ph-BTZ is tribo-positive. Building on our findings, we engineered PDMS/MXene composite films with varying MXene loadings and coupled them with TPA-Ph-BTZ to explore synergistic charge-generation mechanisms. Comprehensive measurements, including electrical output, surface potential, dielectric constant, and wettability, revealed that MXene reinforcement significantly enhances the charge-storage ability and effective contact behavior of PDMS. The TPA-Ph-BTZ-PDMS/MXene (2 wt %) TENG delivered the highest electrical output of ∼290 V, ∼100 μA, and a power density of 2.77 W/m^2. The device also showed stable operation over 10,000 test cycles, confirming its mechanical robustness. Further, an optimized TENG was used in powering a series-connected 240 LEDs. Beyond energy harvesting, the high-voltage output of the TPA-Ph-BTZ−PDMS/MXene TENG is further demonstrated for self-powered activation of discharge tubes for neon, establishing an application pathway for triboelectric-driven discharge electronics. This study establishes TPA-Ph-BTZ−MXene/PDMS as a highly efficient triboelectric pairing, offering a design pathway for molecular-material-based TENGs.

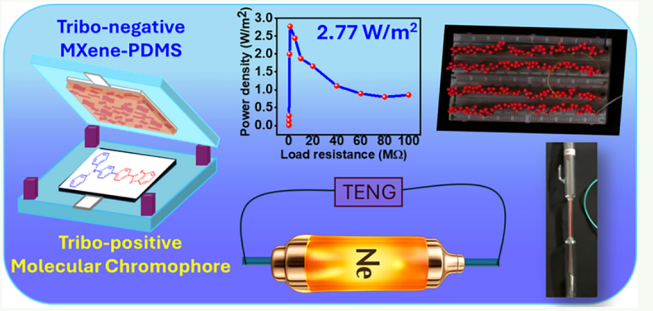

KEYWORDS: *energy harvesting, triboelectric nanogenerator, molecular chromophores, MXene, PDMS nanocomposites, noble-gas discharge*

1. INTRODUCTION

The rapid growth of self-powered electronic systems and sensors has intensified research interest in triboelectric nanogenerators (TENGs).[1−5] TENGs are considered efficient platforms for harvesting low-frequency mechanical energy from both ambient and human activities. Owing to their simple device architecture, multiple modes of operation, material versatility, and high output-voltage characteristics, they are suitable for wearable electronics, self-powered sensors, human−machine interfaces, and distributed Internet-of-Things (IoT) nodes.[6−8] Despite these advantages, the performance and functional scope of TENGs depend on the proper selection of triboelectric material pairs, which becomes a central challenge in exploring new tribo-positive and tribo-negative materials to advance this field.[9−15] In the present work, we have explored a new tribo-positive material, namely, Triphenylamine−phenyl−benzothiazole (TPA-Ph-BTZ).

Molecular and chromophore-based materials are a promising class of triboelectric materials that remain largely unexplored. Their well-defined electronic structures, intrinsic molecular dipoles, and tunable electron-donating and -withdrawing functionalities offer unique opportunities to engineer tribo-electric polarity at the molecular level.[16−18] Triphenylamine−

Received: December 26, 2025
Revised: March 25, 2026
Accepted: March 25, 2026

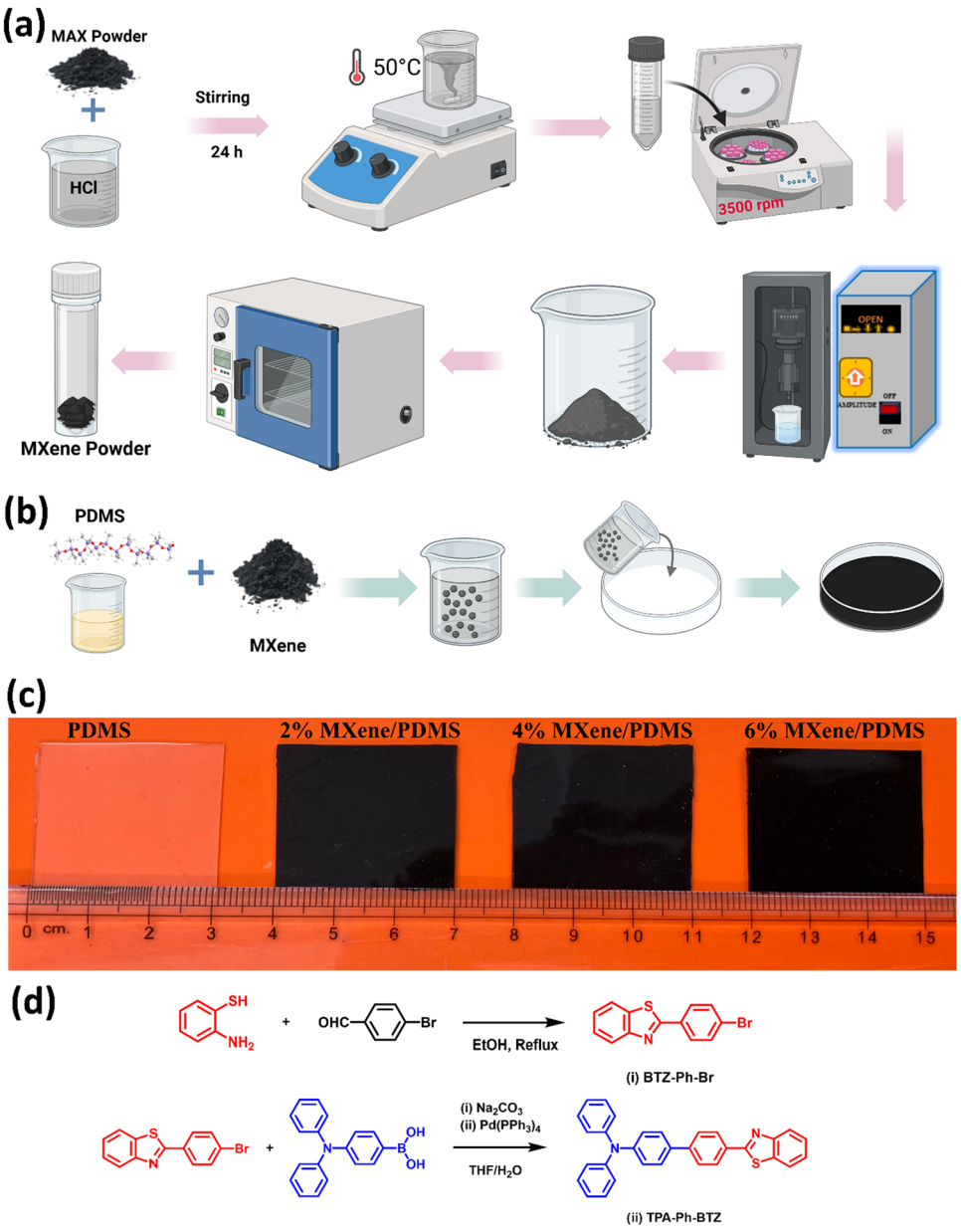

Figure 1. (a) Synthesis procedure of MXene, (b) preparation procedure of PDMS-MXene composites, (c) photographs of the prepared pure PDMS and PDMS-MXene composite films, and (d) synthesis procedure of TPA-Ph-BTZ.

phenyl−benzothiazole (TPA-Ph-BTZ), a donor−π−acceptor (D-π-A) molecular chromophore, is particularly attractive in this context due to the strong electron-donating nature of the triphenylamine unit coupled with the electron-withdrawing benzothiazole moiety, resulting in pronounced intramolecular charge transfer. When employed as the triboelectric layer, the intrinsic dipolar character of TPA-Ph-BTZ biases directional electron transfer at the contact interface, enabling the molecule to exhibit an overall tribo-positive behavior when paired with highly electronegative polymers such as fluorinated ethylene propylene (FEP). In this configuration, electron donation is predominantly governed by the triphenylamine segment, while the benzothiazole moiety assists in stabilizing the separated charges, thereby suppressing back-transfer and enhancing charge retention. TPA-based materials, explored for optoelectronic, electrochromic, and molecular electronic devices, have not yet been systematically investigated as an active triboelectric material.[19−21] Establishing the triboelectric behavior of such D-π-A molecular systems and elucidating their interfacial interactions with polymeric counterparts can open new molecular-level design strategies for high-performance triboelectric nanogenerators.

In recent years, significant efforts have been devoted to enhancing TENG output through surface micro- and nanoscale structuring, dielectric engineering, and the incorporation of functional fillers into polymer matrices.[22−27] Among all strategies, polymer−nanofiller composites have emerged as particularly effective, enabling simultaneous tuning of dielectric constant, charge-trapping capability, and mechanical compliance.[28−33] Two-dimensional (2D) materials, such as MXenes, have attracted growing attention in this context due to their high electrical conductivity, large surface area, and tunable surface terminations.[34−37] The negative triboelectric nature of MXene is well established in the literature, and it can be an

https://doi.org/10.1021/acsaelm.5c02701
ACS Appl. Electron. Mater. XXXX, XXX, XXX−XXX

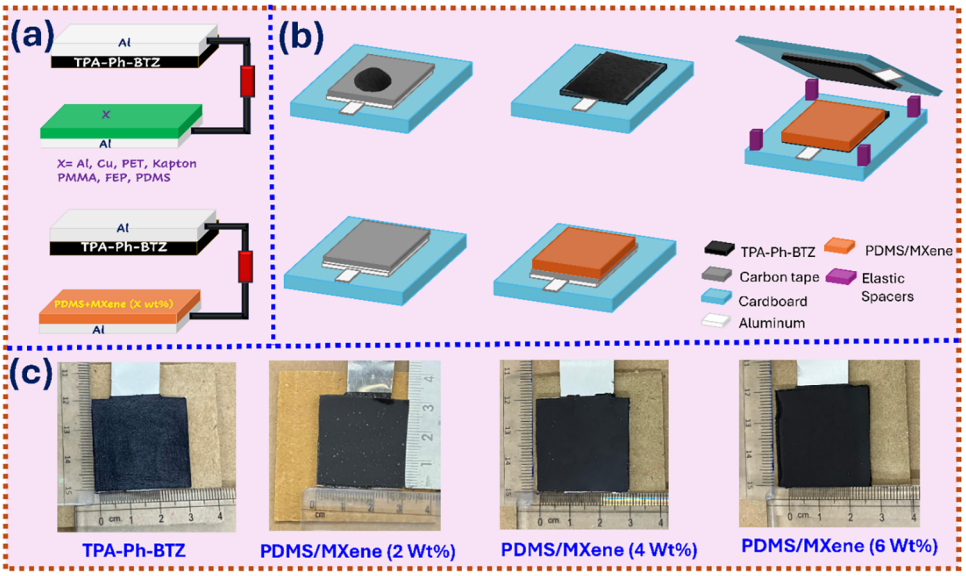

Figure 2. (a) Schematic of the TENG device designs. (b) Device fabrication of PDMS/MXene-TPA-Ph-BTZ TENG; (c) photographs of the few selected frictional layers.

effective filler in tribo-negative polymers to enhance the performance of TENG devices.[28,38] However, most reported studies focus primarily on optimizing the tribo-negative polymer layer, while the exploration of fundamentally new tribo-positive materials remains comparatively limited. In this work, we have explored tribo-negative polymer-MXene composite films with a new tribo-positive material. We report a novel triboelectric pairing between TPA-Ph-BTZ and MXene-reinforced PDMS composites for high-performance TENGs.

In addition to energy harvesting and self-powered sensing, TENGs have recently attracted attention as compact high-voltage sources due to their ability to generate high potentials at low current.[39−42] Such an electrical profile is particularly well suited for gas discharge and plasma-based systems, where a high breakdown voltage is required to initiate ionization, while the sustaining current remains relatively small. Despite this natural compatibility, the use of TENGs for noble-gas discharge activation has remained largely unexplored. In this work, we address this gap by employing a molecular-chromophore-based TPA-Ph-BTZ-PDMS/MXene TENG to activate neon discharge tubes, highlighting a previously unreported application domain for TENG-driven high-voltage electronic systems.

2. EXPERIMENTAL SECTION

2.1. Materials

The MAX (Ti_3AlC_2) phase precursor, 4-bromobenzaldehyde, ethanol, 2-aminobenzenethiol, 2-(4-bromophenyl) benzo[*d*]thiazole (3 mmol), 4-(diphenyl amino)phenylboronic acid (3 mmol), and Na_2CO_3 were purchased from Sigma-Aldrich, while hydrofluoric acid (HF) and other basic chemicals were sourced from SRL Chemicals. poly(dimethylsiloxane) (PDMS, Sylgard TM184) was purchased from Dow Corning Corp. All materials and chemicals were used as received without additional purification.

2.2. Synthesis of TPA-Ph-BTZ

2.2.1. 2-(4-Bromophenyl)benzo[*d*]thiazole (BTZ-Ph-Br). 4-Bromobenzaldehyde (2.161 mmol) in ethanol, and 2-aminobenzenethiol (2.378 mmol) were taken into the Rb flask, and ethanol (30 mL) was added to the mixture and stirred overnight at 75 °C. After the reaction was completed, the mixture was cooled to room temperature and then poured into ice water, which formed a precipitate, and the mixture was filtered.[43] The dried precipitate was collected from the filter paper and then purified by column chromatography; finally, we obtained the white solid.; 1H NMR ($CDCl_3$, 400 MHz): δ 8.00 (1H, d), 7.90 (2H, d), 7.84 (1H, d), 7.57 (2H, d), 7.43 (1H, t), 7.33 (1H, t). (Supporting Information (SI), Figure S1).

2.2.2. 4′-(Benzo[*d*]thiazol-2-yl)-*N*,*N*-diphenyl-[1,1′-biphenyl]-4-amine (TPA-Ph-BTZ). A mixture of 2-(4-bromophenyl)benzo-[*d*]thiazole (3 mmol), 4-(diphenyl amino)phenylboronic acid (3 mmol), Na_2CO_3 (9 mmol), and $Pd(PPh_3)_4(0)$ (0.24 mmol) was dissolved in THF and H_2O (v/v = 3:1, 45 mL) and stirred at 85 °C for 24 h, under neutral atmosphere by nitrogen gas. After that, the mixture was extracted with dichloromethane and water.[44] The concentric mixture under rotavapor was the crude product, which was purified by column chromatography. ^{1}H NMR ($CDCl_3$, 400 MHz): δ 8.15 (2H, d), 8.09 (1H, d), 7.92 (1H, d), 7.71 (2H, d), 7.55 (2H, d), 7.50 (1H, t), 7.39 (1H, t), 7.29 (4H, m), 7.16 (6H, m), 7.06 (2H, t). The NMR spectra of TPA-Ph-BTZ are provided in SI Figure S2.

2.3. Preparation of MXene and MXene Composite Films

Figure 1(a) illustrates the synthesis procedure for the MXene from the MAX phase, which is similar to the reported literature.[45] Typically, 1 g of MAX-phase powder is stirred with aqueous hydrofluoric acid (HF) (20 mL) at room temperature for 24 h. As a result, Aluminum layers were selectively etched out, and metallic bonds between MX layers were replaced with surface-terminated hydroxy, fluoride, or oxygen on the surface. The resulting etched powder was repeatedly washed by centrifugation at 3500 rpm for 5 min per cycle, for a total of 6 cycles, until the solution reached a neutral pH of 6, ensuring complete removal of residual acid. Subsequently, the washed MXene is treated with 20 mL of DMSO and stirred at room temperature to help the solvent intercalate between the $Ti_3C_2T_x$ layers. The excess DMSO is then removed by 6 additional centrifugation cycles at 3500 rpm for 5 min, yielding purified intercalated MXene. The obtained etched MXene material is dispersed in 160 mL of deionized water and sonicated with a probe sonicator at room temperature for 6 h to achieve delamination into few-layer MXene nanosheets. Subsequently, the delaminated MXene dispersion is vacuum-dried at 80 °C for 18 h to produce dry MXene powder for subsequent use.

To prepare the PDMS-MXene composite film, a clean Petri dish served as the casting surface. For preparing the pure PDMS film, 5 g of PDMS elastomer base was combined with 0.5 mL of curing agent

https://doi.org/10.1021/acsaelm.5c02701
ACS Appl. Electron. Mater. XXXX, XXX, XXX−XXX

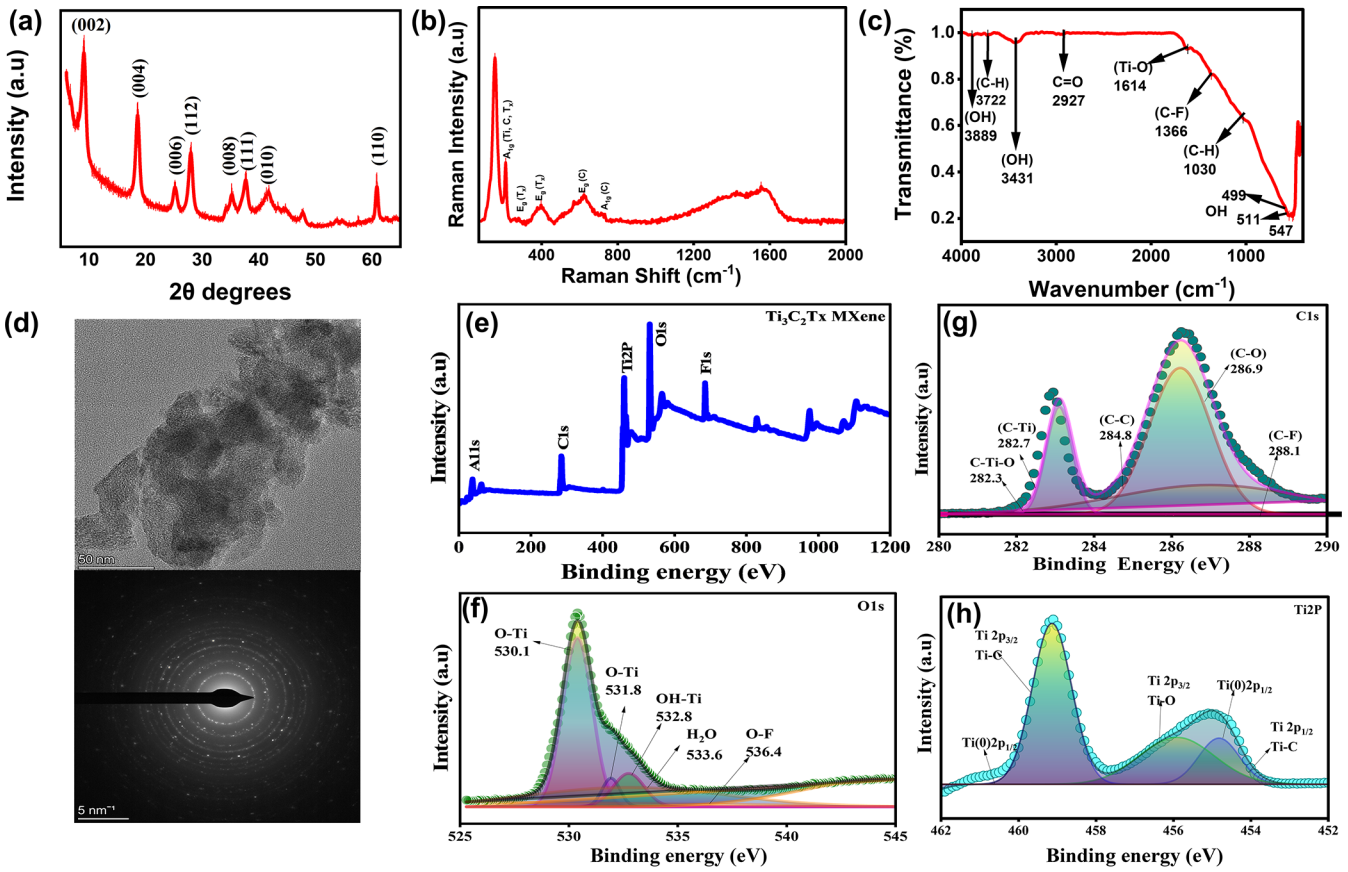

Figure 3. Characterization of MXene pure sample: (a) XRD, (b) Raman, (c) FTIR, (d) TEM, and (e–h) XPS.

and stirred manually with a glass rod for 20 min to achieve a uniform mixture. This mixture was then poured into the cleaned Petri dish and cured in a hot-air oven at 45 °C to produce a consistent PDMS film, as shown in Figure 1(b). To create MXene-PDMS composite films, MXene powder was added to the PDMS at various weight fractions (1, 2, 3, 4, and 6 wt %) and thoroughly mixed for even dispersion. Each mixture was poured into a cleaned Petri dish and cured at 45 °C under the same conditions. After curing, flexible, freestanding MXene-PDMS composite films were obtained. The as-synthesized PDMS-MXene composite films are depicted in Figure 1c. The detailed synthesis procedure of TPA-Ph-BTZ is depicted in Figure 1d.

2.4. Materials Characterization

The structural and morphological characteristics of the samples were investigated using X-ray diffraction (XRD, X'Pert Powder) and field-emission scanning electron microscopy (FESEM, JEOL JSM-IT800) equipped with an energy-dispersive X-ray spectroscopy (EDS) detector. The functional groups present in the samples were analyzed by Fourier transform infrared spectroscopy (FTIR, Shimadzu 8201 PC). Optical properties were examined by using diffuse reflectance UV–vis spectroscopy (Agilent Technologies, Cary 5000). Contact-angle measurements were performed by placing a 10 μL droplet of deionized water onto the sample surface using an APEX (ACAM MSC) goniometer. The contact angles were measured before and after aging. For each sample, five independent measurements were recorded, and their average was used for comparison. The dielectric measurements were performed using an LCR meter (HIOKI; Model 3532, Japan) in the frequency range from 100 Hz–1 MHz. The surface potential measurements were performed using TRek (Electrostatic Voltage Model 542A).

2.5. Fabrication and Electrical Characterization of TENGs

In this work, two sets of TENG devices were fabricated using prepared TPA-Ph-BTZ powder and Silicone/MXene composite films. A schematic of the fabricated TENG devices in the vertical contact-separation mode is shown in Figure 2(a). In the first set, the TPA-Ph-BTZ layer was kept as the fixed tribo-positive contact layer, while the opposite friction layers, such as Al, Cu, PET, Kapton, PMMA, FEP, and silicone rubber, were varied for each device to confirm the triboelectric nature of TPA-Ph-BTZ. Initially, a double-sided conductive carbon tape was attached onto a predesigned aluminum substrate, and TPA-Ph-BTZ powder was uniformly deposited on the carbon tape by gentle pressing. Loosely bound particles were removed by using an air blower. This deposition process was repeated several times until a continuous TPA-Ph-BTZ film completely covered the carbon tape. The uniformity of the coating was confirmed by measuring the surface resistance at multiple points, which consistently showed high resistance, indicating complete coverage of the conductive tape by the TPA-Ph-BTZ layer. This approach offers several advantages, including (a) preserving intrinsic molecular surface properties without dilution in a polymer matrix, (b) enabling direct evaluation of its triboelectric polarity, (c) providing good electrical contact through the conductive substrate, and (d) facilitating rapid prototyping and material screening.

The TPA-Ph-BTZ-coated aluminum substrate was then fixed onto the predesigned cardboard frame and kept aside for device assembly. The photograph of the prepared friction layers is presented in Figure 2(c). For each opposite friction layer, the respective material (Al, Cu, PET, Kapton, PMMA, FEP, or silicone rubber) was separately mounted on an aluminum substrate using carbon tape and then attached to a similar cardboard frame. Each combination of TPA-Ph-BTZ with a different friction layer constituted a new TENG device. To assemble the device, sponge spacers were positioned at the four corners of one of the support cards to maintain a uniform air gap (~1.2 cm) between the two frictional layers. These elastic spacers act as restoring elements, enabling the layers to separate automatically after each contact during mechanical tapping.

In the second set of TENG devices, the TPA-Ph-BTZ layer was again used as the fixed friction layer, while pure PDMS and PDMS/

https://doi.org/10.1021/acsaelm.5c02701
ACS Appl. Electron. Mater. XXXX, XXX, XXX–XXX

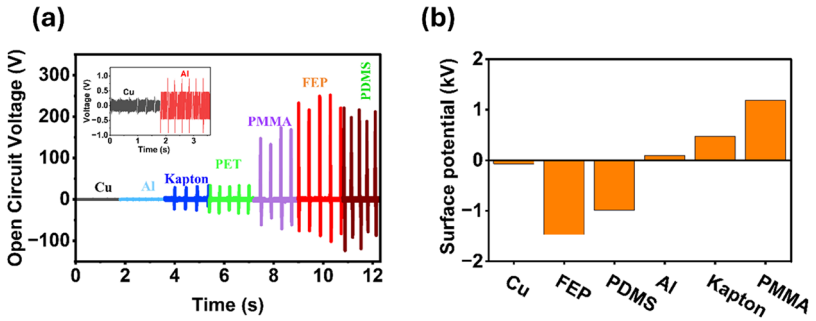

Figure 4. (a) Electrical output of TPA-Ph-BTZ-based TENG devices with different opposite frictional layers; (b) surface potential of different frictional layers after contacting with the TPA-Ph-BTZ layer.

MXene composite films (with MXene loadings of 1, 2, 3, 4, and 6 wt %) were used as the opposite tribolayers, as shown in Figure 2(b). The preparation of the TPA-Ph-BTZ layer followed the same procedure described above. The PDMS and composite films were attached onto predesigned aluminum substrates using carbon tape, ensuring firm electrical connection and mechanical support. Each pairing of TPA-Ph-BTZ with a different PDMS/MXene composite film formed a new TENG device for performance comparison.

The electrical performance of the fabricated TENGs was tested under hand-tapping-induced biomechanical excitation at a frequency of approximately 4−5 Hz, under ambient laboratory conditions (RH ∼45%, Temperature ∼27 °C). The open-circuit voltage (V_{oc}) and short-circuit current (I_{sc}) were recorded using a digital storage oscilloscope (DSO) and a low-noise current preamplifier (Stanford Research Systems, SR-570), respectively. The transferred charge was measured using an electrometer (Keithley 6517B). The load-dependent output characteristics were determined using a decade resistance box, while long-term durability was assessed using an in-house-developed linear motor setup that operated for over 10,000 continuous contact−separation cycles.

3. RESULTS AND DISCUSSION

The XRD pattern of pure MXene powder is shown in Figure 3a; the XRD peaks appearing at 9.04°, 18.6°, 25.19°, 28.03°, 35.16°, 37.75°, 41.75°, and 60.87° correspond to (002), (004), (006), (112), (008), (111), (010), and (110) planes. These diffraction peaks are consistent with the reported literature for MXene.[2,28,46,47] The Raman spectrum of the MXene sample is shown in Figure 3b. The Raman spectrum of MXene aligns with the previously reported peaks; the peak at 210 cm^{-1} is attributed to A_{1g} (Ti, C, T_x), while the peak at 350−650 cm^{-1} is assigned to E_g (T_x) and E_g (C). The peak around 722 cm^{-1} is A_{1g} (C).[48,49] The FTIR spectrum of $Ti_3C_2T_x$ MXene confirms successful MAX-phase etching and surface functionalization (shown in Figure 3c). The broad bands at 3889 = 3431 cm^{-1} arise from O−H stretching of surface −OH groups and interlayer-confined water, while the weak feature at ∼3722 cm^{-1} and the band at ∼2927 cm^{-1} correspond to C−H stretching vibrations. The absorption at ∼1614 cm^{-1} is mainly attributed to C−O/Ti−O related vibrations associated with oxygen terminations. The peak at ∼1366 cm^{-1} confirms C−F stretching, indicating fluorine surface terminations introduced during HF etching, and the feature at ∼1030 cm^{-1} is assigned to C−H and C−O bending modes. In the fingerprint region, the bands at ∼547−499 cm^{-1} correspond to Ti−O and Ti−C vibrations, which are characteristic of $Ti_3C_2T_x$ MXene. Overall, the observed vibrational modes are in excellent agreement with reported MXene FTIR signatures and confirm the formation of surface-terminated $Ti_3C_2T_x$.[48,50] The TPA-Ph-BTZ material characterization details, such as FTIR and XPS, are provided in SI Figure S3.

Figure 3d shows the transmission electron microscopy (TEM) of the MXene powder. The TEM image shows thin, sheet-like $Ti_3C_2T_x$ nanosheets with lateral dimensions of a few tens of nanometers, confirming effective delamination of the MXene. The lack of dense particles or thick stacks suggests successful exfoliation without significant restacking. The SAED pattern displays clear concentric diffraction rings, typical of a polycrystalline layered structure that maintains in-plane order. No diffraction rings from crystalline TiO_2 are present, indicating that the MXene remains structurally intact with minimal bulk oxidation. The XPS survey spectrum (Figure 3e) confirms the presence of Ti, C, and F, while no Al peaks are detected, indicating that the Al layer was completely removed from the MAX phase. The O 1s spectrum (Figure 3f) shows mixed surface terminations, with the O−Ti and OH−Ti components confirming −O/−OH functionalization, along with minor signals from adsorbed water or the O−F species. The C 1s spectrum (Figure 3g) is dominated by the Ti−C peak at 282.7 eV, which uniquely identifies $Ti_3C_2T_x$ MXene; minor C−C and C−O signals are attributed to surface defects and partial oxidation. The Ti 2p spectrum (Figure 3h) displays strong Ti−C peaks with only a weak Ti^{4+} contribution, suggesting that oxidation largely occurs only on the surface and the carbide structure of the MXene remains mostly intact. The XRD and Raman spectra of PDMS/MXene composites are presented in SI Figure S4. The PDMS/MXene composite exhibits a broader, less intense MXene (002) XRD peak than pure MXene, indicating inhibited restacking during polymer infiltration while maintaining the layered architecture. Raman spectra show that MXene vibrational modes continue with diminished intensity alongside prominent PDMS bands, confirming successful embedding and robust interfacial bonding without damaging MXene's structure.

3.1. Determination of Triboelectric Nature of TPA-Ph-BTZ

Based on the electronic structure and bonding characteristics of TPA-Ph-BTZ, it can be considered a potential candidate for tribo-positive materials. To validate this hypothesis, the first set of TENG devices (TPA-Ph-BTZ paired with different frictional layers) was evaluated under hand-tapping conditions, and the corresponding electrical outputs are shown in Figure 4(a). The results clearly indicate that TPA-Ph-BTZ generates comparatively lower voltage when paired with standard tribo-positive layers, whereas significantly higher output is observed when PTZ is paired with well-known tribo-negative materials. This trend confirms the tribo-positive nature of TPA-Ph-BTZ.

https://doi.org/10.1021/acsaelm.5c02701
ACS Appl. Electron. Mater. XXXX, XXX, XXX−XXX

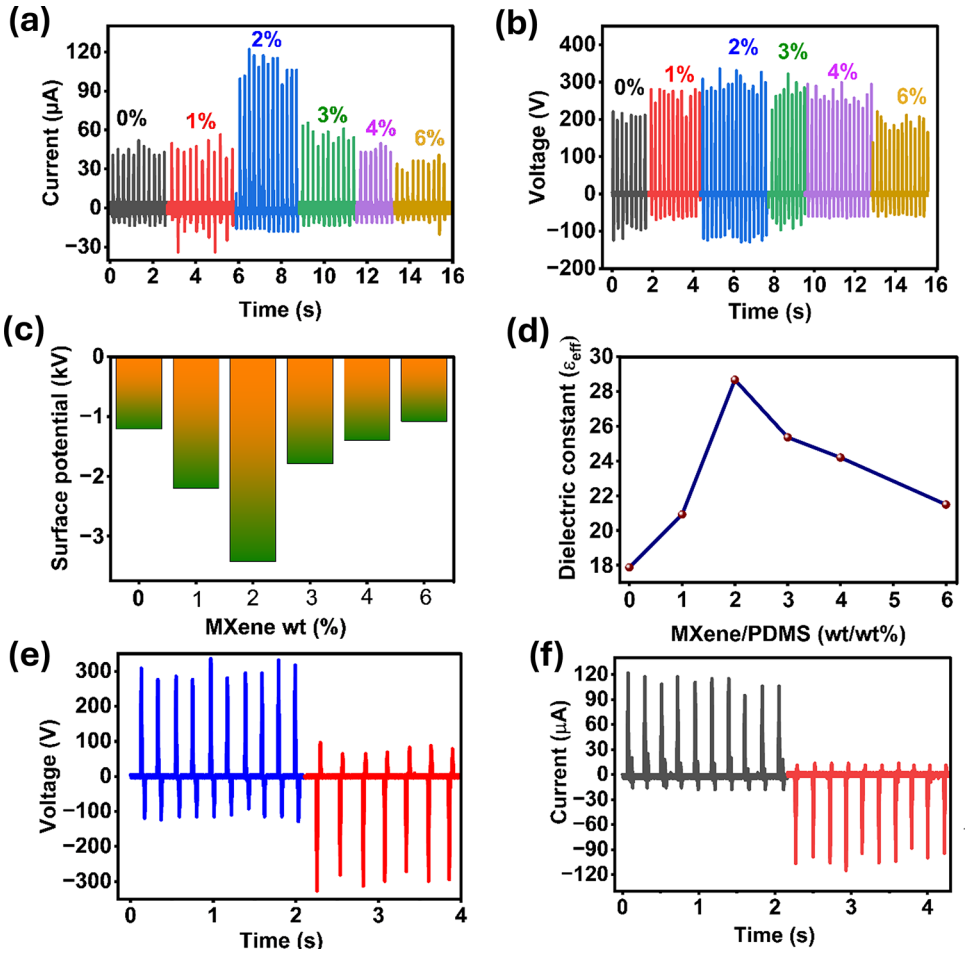

Figure 5. Electrical output performance of PDMS/MXene-TPA-Ph-BTZ-based TENGs with different percentages of MXenes: (a) I_{sc} and (b) V_{oc}, PDMS/MXene films (c) surface potential, (d) dielectric constant, switching polarity test outputs (e) V_{oc}, (f) I_{sc}.

To further support this conclusion, the surface potential of all frictional layers was measured after contact with TPA-Ph-BTZ, and the results are presented in Figure 4(b). As expected, FEP and PDMS exhibited negative surface potential after contact, indicating that PTZ acquired a positive surface potential characteristic of tribo-positive materials. Interestingly, Al, Kapton, and PET showed positive surface potentials, suggesting that PTZ behaves as an electron-accepting material in these pairs. In contrast, when paired with Cu, PTZ acted as an electron donor, resulting in Cu acquiring a smaller negative potential.

It is well-known that the position of a material in the triboelectric series is determined by its electron affinity, which is further influenced by multiple factors, including work function, surface chemistry, roughness, dielectric constant, and film thickness. Therefore, it is challenging to assign an absolute position to TPA-Ph-BTZ within the triboelectric series. Nevertheless, the combined electrical output and surface potential results clearly place TPA-Ph-BTZ on the positive side of the triboelectric series.

3.2. Energy-Harvesting Properties of PDMS/MXene-TPA-Ph-BTZ TENG Devices

Based on the earlier results, TPA-Ph-BTZ–FEP and TPA-Ph-BTZ–PDMS pairs produced the highest electrical outputs, confirming that TPA-Ph-BTZ performs exceptionally well when combined with tribo-negative materials. To further enhance the performance of TPA-Ph-BTZ-based TENGs, we explored incorporating MXene into a PDMS matrix, as PDMS offers easy processability, high flexibility, and greater mechanical durability than FEP. In this section, TPA-Ph-BTZ was paired with a series of PDMS/MXene composite films with varying MXene loadings, and the corresponding TENG device outputs under hand tapping are shown in Figure 5(a),(b).

The current and voltage responses clearly show that the PDMS/MXene-TPA-Ph-BTZ (2 wt %) device exhibits the highest performance, delivering an open-circuit voltage of ~290 V and a short-circuit current of ~100 μA. All composite-based devices follow the characteristic trend observed in polymer–nanofiller TENG systems reported in the literature, where an optimal filler concentration maximizes triboelectric output.[51−55]

The superior performance of the PDMS/MXene-TPA-Ph-BTZ (2 wt %) device can be understood by evaluating its surface potential and dielectric properties. As shown in Figure 5(c), the surface potential measured after contact with TPA-Ph-BTZ is highest for the 2 wt % MXene composite film, indicating the strongest charge-accumulation capability in this film. This correlates well with the enhanced output voltage and current observed for this pair. Dielectric constant measurements shown in Figure 5(d) further support this trend, revealing that the composite containing 2 wt % MXene exhibits the maximum ε_{eff} among all composite films. A higher dielectric constant improves charge storage and reduces charge

https://doi.org/10.1021/acsaelm.5c02701
ACS Appl. Electron. Mater. XXXX, XXX, XXX−XXX

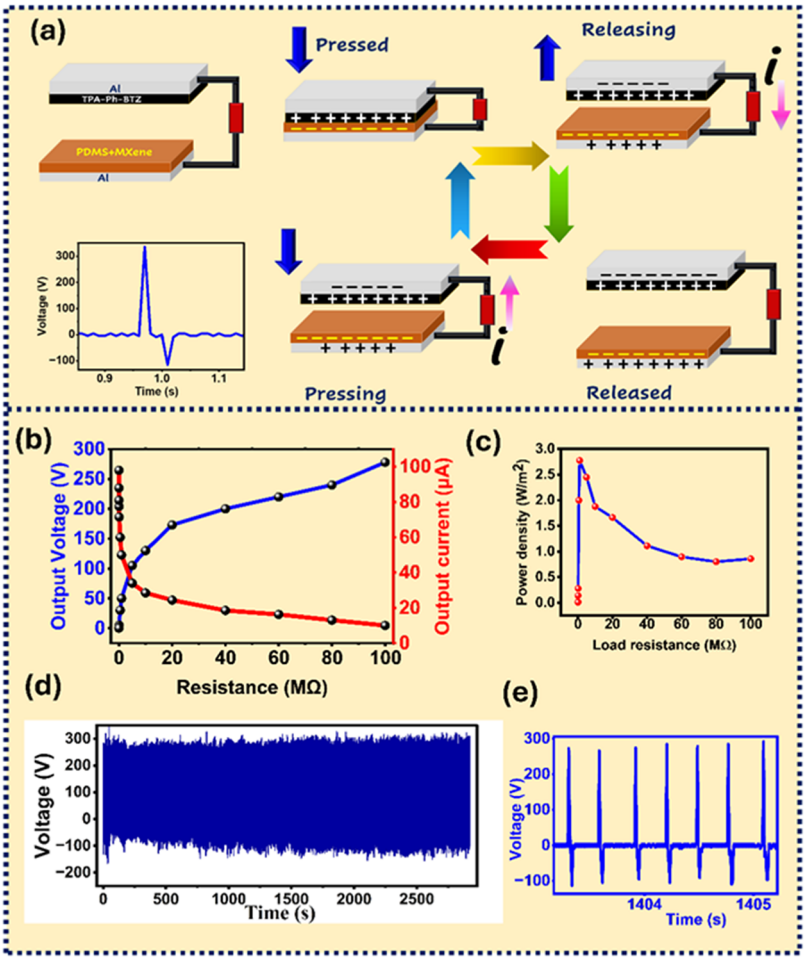

Figure 6. (a) Working mechanism of PMZ-2 TENG, PMZ-2 TENG (b) load characteristics, (c) power density, (d) long-term stability, and (e) magnified view of a few cycles from stability.

leakage, resulting in an enhanced triboelectric output. Further hydrophobicity of all of the composite films is recorded and presented in SI Figure S5. Although contact-angle measurements show a slightly higher hydrophobicity for the 2 wt % composite film, the variations in surface wettability from 92 to 95° across all samples are relatively small. Therefore, the influence of contact angle on output performance is expected to be minimal compared to the dominant contributions from the dielectric and surface potential effects. From the combined analysis of electrical output, surface potential, dielectric behavior, and contact-angle data, it can be concluded that TPA-Ph-BTZ paired with PDMS/MXene (2 wt %) (PMZ-2 TENG) is the optimal combination, and this pair was selected for detailed investigation of subsequent TENG characteristics. Figure 5(e),(f) shows the switching polarity test outputs of the selected TENG, and they confirm the electrical output generated from the TENG, not from any noise. The transferred charge was measured using an electrometer for the PDMS/MXene-TPA-Ph-BTZ (2 wt %) device and presented in SI Figure S6. The transferred charge was found to be nearly 60 nC between the two active electrodes. The PDMS/MXene-TPA-Ph-BTZ-based TENG device was further optimized by increasing the separation between the two electrodes, and the output was generated by different human touch inputs and frequencies. The detailed results are presented in SI Figure S7.

Figure 6(a) elucidates the working mechanism of PMZ-2 TENG, in which the PDMS-MXene layer acts as an electron acceptor, and TPA-Ph-BTZ acts as an electron donor material. When periodic hand tapping is applied, the TPA-Ph-BTZ and PDMS/MXene friction layers undergo repeated contact and separation. During the contact stage, charge transfer occurs due to their difference in triboelectric polarity: the TPA-Ph-BTZ layer donates electrons and becomes positively charged, while the PDMS/MXene composite accepts electrons and acquires a negative charge. Upon release of the applied force, the layers separate, generating a time-dependent potential gradient that drives electron flow through the external circuit until an equilibrium state is reached at the maximum separation distance. When the layers are brought into contact again, the potential difference reverses, causing electrons to flow in the opposite direction. This continuous sequence of contact−separation cycles under hand tapping produces an alternating electrical output, as reflected in the representative waveform in Figure 6(a).

Figure 6(b,c) presents the load characteristics of the TENG, highlighting the conditions required for maximum instantaneous power delivery. The output voltage increases sharply with load resistance and reaches a saturation value of ∼280 V at higher resistances, which is consistent with reduced charge dissipation under high-impedance conditions. In contrast, output current decreases progressively as the load resistance increases, following the characteristic impedance-dependent

https://doi.org/10.1021/acsaelm.5c02701
ACS Appl. Electron. Mater. XXXX, XXX, XXX−XXX

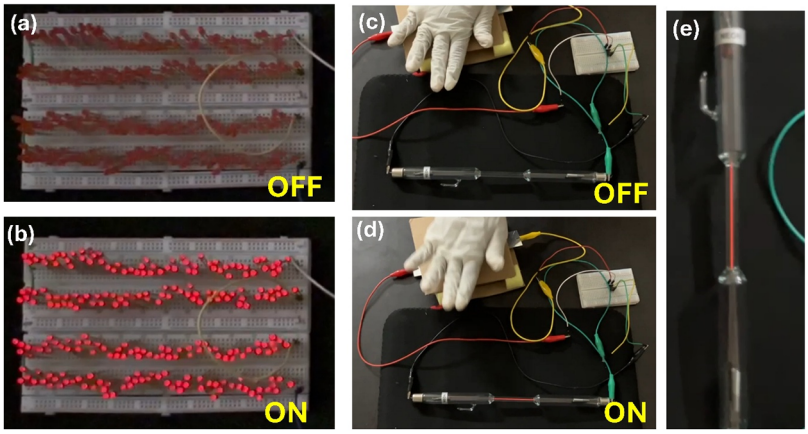

Figure 7. Photograph of the (a, b) series-connected LEDs in OFF and ON state; (c–e) discharge tube in ON and OFF state, and magnified view.

behavior of TENGs. Using the measured load data, the instantaneous power density was calculated using $P = \frac{V^2}{(R_L \times A)}$ and is shown in Figure 6(c). The TENG exhibits a distinct peak power density of 2.77 W m^{-2} at an optimal load of 1 MΩ, indicating favorable impedance matching and efficient charge-transfer dynamics. At load resistances beyond this optimum, the power output gradually decreases due to increased energy-loss limitations associated with excessively high external resistance. The long-term operational stability of the PMZ-2 TENG was evaluated over 10,000 continuous contact–separation cycles, and the corresponding voltage output is presented in Figure 6(d), with a magnified view of selected cycles shown in Figure 6(e). As is evident from the recorded responses, the PMZ-2 TENG exhibits highly consistent and repeatable voltage output throughout the entire cycling duration, without noticeable degradation or fluctuation. This stable electrical performance confirms the excellent mechanical robustness of the device and demonstrates the long-term reliability of its energy-harvesting capability. The effect of humidity was measured (SI Figure S8), and it is observed that TENG output is decreased with increasing humidity level due to surface charge dissipation by the presence of water molecules, and the same trend is reported by many research groups.[56,57] Furthermore, a detailed literature comparison of MXene-based TENG devices performance is provided in SI Table S1.

3.3. Applications of PMZ-2 TENG

The practical applicability of the PMZ-2 TENG was first evaluated by powering 240 LEDs connected in series under simple mechanical hand-tapping excitation. Photographs of the LED array in the OFF and ON states are shown in Figure 7(a,b), and the corresponding real-time operation is provided in SI Video V1.

To further demonstrate the capability of the PMZ-2 TENG as a self-powered high-voltage source, its electrical output was employed to activate a noble-gas discharge tube filled with neon (Ne). In the Ne discharge tube, electrodes are separated by 16.5 cm, and the center tube diameter is ∼6 mm (SI Figure S9). In this configuration, the alternating triboelectric output was first passed through a full-wave bridge rectifier, producing a unidirectional high-voltage signal (SI Figure S9) that was directly applied to the discharge tube, as shown in Figure 7(c). Under periodic hand-tapping excitation, the rectified high-voltage pulses generated by the TENG were sufficient to exceed the breakdown voltage of Ne gas, resulting in the clearly visible discharge emission shown in Figure 7(d,e), without the assistance of any external power supply. This observation confirms that the developed TENG can deliver the high electric field strength required for gas ionization, despite operating in the microampere current regime. Photographs of the noble-gas discharge tube in the OFF and ON states, powered exclusively by the TENG, are presented in Figure 7(c,d), while real-time demonstrations are provided in SI Video V2. To further demonstrate the generality of this high-voltage activation capability, a helium (He) discharge tube of comparable dimensions was also tested. Under identical hand-tapping excitation conditions, a clearly visible glow discharge was observed in the helium tube as well, confirming that the prepared TENG can reliably initiate ionization across different noble gases. Real-time operation of the helium discharge emission is provided in the SI Video V3.

This study introduces TENGs as viable self-powered, high-voltage excitation sources for noble-gas discharge systems, thereby establishing a new interface between TENG technology and plasma electronics. Although the present work is limited to discharge ignition rather than sustained plasma operation, it clearly demonstrates the feasibility of employing molecular chromophore–polymer nanocomposite-based TENGs for self-powered gas discharge activation. This capability positions the PDMS/MXene-TPA-Ph-BTZ TENG as a promising candidate for intermittent high-voltage applications, including plasma indicators, leakage detection systems, safety-signaling devices, and educational plasma sources, where compactness, electrical isolation, and elimination of external power supplies are particularly advantageous.

4. CONCLUSIONS

In this study, we demonstrate a new and effective triboelectric pairing between TPA-Ph-BTZ and MXene-reinforced PDMS composites for high-performance TENGrs. A systematic assessment of TPA-Ph-BTZ against standard triboelectric materials confirms its innate tribo-positive character, thereby establishing its suitability as a donor material in TENG configurations. The second set of devices fabricated using TPA-Ph-BTZ and PDMS/MXene composite films shows that MXene addition significantly improves the dielectric properties, charge-accumulation capacity, and interfacial contact efficiency of the PDMS layer. Among all devices, the PDMS/MXene-TPA-Ph-BTZ (2 wt %) device delivered the highest

https://doi.org/10.1021/acsaelm.5c02701
ACS Appl. Electron. Mater. XXXX, XXX, XXX–XXX

electrical performance, reaching approximately 290 V, around 100 μA, and a peak power density of 2.77 W m^{-2} under hand-tapping excitation. A detailed analysis of surface potential, dielectric constant, and wettability confirms that the synergistic combination of TPA-Ph-BTZ's strong electron-donating nature and the enhanced charge-storage capacity of the MXene-modified PDMS matrix enables superior output generation. Overall, this study establishes PDMS/MXene-TPA-Ph-BTZ as a promising triboelectric pair, demonstrating both high output performance and stable operation during extended mechanical cycling. The results offer new insights into the application of molecular-chromophore-based materials in triboelectric devices and highlight MXene−polymer nanocomposites as adaptable, scalable friction layers for next-generation energy-harvesting systems.

■ ASSOCIATED CONTENT

Supporting Information

The Supporting Information is available free of charge at https://pubs.acs.org/doi/10.1021/acsaelm.5c02701.

Powering LEDs (Video V1) (MP4)

Powering neon discharge tube (Video V2) (MP4)

Powering helium discharge tube (Video V3) (MP4)

NMR spectra of BTZ-Ph-Br and TPA-Ph-BTZ (Figures S1 and S2); synthesis of TPA-Ph-BTZ (Figure S3); XRD and Raman spectra of PDMS/MXene (2%) composite film (Figure S4); and contact angles of PDMS/MXene composite films (Figure S5) (PDF)

■ AUTHOR INFORMATION

Corresponding Authors

Uday Kumar Khanapuram − *Department of Physics, Energy Materials and Devices (EMD) Lab, National Institute of Technology, Warangal 506004, India;* orcid.org/0000-0003-1297-4104; Email: kanapuram.udaykumar@nitw.ac.in

Rakesh Kumar Rajaboina − *Department of Physics, Energy Materials and Devices (EMD) Lab, National Institute of Technology, Warangal 506004, India;* orcid.org/0000-0003-4023-9051; Email: rakeshr@nitw.ac.in

Authors

Suman Mudu − *Department of Physics, Kakatiya University, Warangal 506009, India; Department of Physics, Energy Materials and Devices (EMD) Lab, National Institute of Technology, Warangal 506004, India*

Vijaykumar Chuncha − *Artificial Photosynthesis Laboratory, Department of Chemistry, National Institute of Technology, Warangal 506004 Telangana, India*

M. Navaneeth − *Department of Physics, Energy Materials and Devices (EMD) Lab, National Institute of Technology, Warangal 506004, India*

Pembarthi Raju − *Department of Physics, Energy Materials and Devices (EMD) Lab, National Institute of Technology, Warangal 506004, India*

Kamakshaiah Charyulu Devarayapalli − *Department of Environmental Engineering, Kyungpook National University, Daegu 41566, Republic of Korea;* orcid.org/0000-0002-7137-6174

Raghu Chitta − *Artificial Photosynthesis Laboratory, Department of Chemistry, National Institute of Technology, Warangal 506004 Telangana, India;* orcid.org/0000-0003-1383-1164

Manjula G − *Department of Physics, Kakatiya University, Warangal 506009, India*

Palash Mishra − *Department of Electrical Engineering, National Institute of Technology, Warangal 506004 Telangana, India*

Dae Sung Lee − *Department of Environmental Engineering, Kyungpook National University, Daegu 41566, Republic of Korea;* orcid.org/0000-0003-3579-0076

Complete contact information is available at: https://pubs.acs.org/10.1021/acsaelm.5c02701

Notes

The authors declare no competing financial interest.

■ ACKNOWLEDGMENTS

The authors, R.K.R. and U.K.K., thank the Director of the National Institute of Technology − Warangal for his constant encouragement and infrastructure support. R.R.K. and K.U.K. acknowledge DAE-BRNS (59/14/06/2024-BRNS/717) for the surface potential measurement system (electrostatic voltmeter) and electrometer (6517B) for charge measurement. S.M. and M.G. acknowledge RUSA 2.0 (Rashtriya Uchchatar Shiksha Abhiyan) for funding.

■ REFERENCES

(1) Anbalagan, S.; Manojkumar, K.; Muthuramalingam, M.; Hajra, S.; Panda, S.; Sahu, R.; Kim, H. J.; Sundaramoorthy, A.; Nithyavathy, N.; Vivekananthan, V. Progress and Recent Advances in Self-Powered Gas Sensing Based on Triboelectric and Piezoelectric Nanogenerators. *Chem. Eng. J.* **2024**, *497*, No. 154740.

(2) Madathil, N.; Babu, A.; Velupula, M.; Kulandaivel, A.; Rajaboina, R. K.; Khanapuram, U. K.; Devarayapalli, K. C.; Lee, D. S. A Layered Double Hydroxides/MXene Composite Based Triboelectric Nanogenerator for Energy Harvesting and Self-Powered Electroplating Applications. *Sustainable Energy Fuels* **2025**, *9* (16), 4364−4374.

(3) Dai, X.; Wu, X.; Yao, B.; Hong, Z.; Jiang, T.; Wang, Z. L. Triboelectric Nanogenerators Powered Hydrogen Production System Using MoS_2/Ti_3C_2 as Catalysts. *Adv. Funct. Mater.* **2024**, *34* (41), No. 2406188.

(4) Wang, J.; Wu, H.; Wang, Z.; He, W.; Shan, C.; Fu, S.; Du, Y.; Liu, H.; Hu, C. An Ultrafast Self-Polarization Effect in Barium Titanate Filled Poly(Vinylidene Fluoride) Composite Film Enabled by Self-Charge Excitation Triboelectric Nanogenerator. *Adv. Funct. Mater.* **2022**, *32* (35), No. 2204322.

(5) Chakraborthy, A.; Nuthalapati, S.; Nag, A.; Altinsoy, M. E.; He, S. Graphene-Based Triboelectric Nanogenerators for Energy-Harvesting Applications. *Sens. Actuators, A* **2024**, *380*, No. 116046.

(6) Choi, D.; Lee, Y.; Lin, Z.-H.; Cho, S.; Kim, M.; Ao, C. K.; Soh, S.; Sohn, C.; Jeong, C. K.; Lee, J.; Lee, M.; Lee, S.; Ryu, J.; Parashar, P.; Cho, Y.; Ahn, J.; Kim, I.-D.; Jiang, F.; Lee, P. S.; Khandelwal, G.; Kim, S.-J.; Kim, H. S.; Song, H.-C.; Kim, M.; Nah, J.; Kim, W.; Menge, H. G.; Park, Y. T.; Xu, W.; Hao, J.; Park, H.; Lee, J.-H.; Lee, D.-M.; Kim, S.-W.; Park, J. Y.; Zhang, H.; Zi, Y.; Guo, R.; Cheng, J.; Yang, Z.; Xie, Y.; Lee, S.; Chung, J.; Oh, I.-K.; Kim, J.-S.; Cheng, T.; Gao, Q.; Cheng, G.; Gu, G.; Shim, M.; Jung, J.; Yun, C.; Zhang, C.; Liu, G.; Chen, Y.; Kim, S.; Chen, X.; Hu, J.; Pu, X.; Guo, Z. H.; Wang, X.; Chen, J.; Xiao, X.; Xie, X.; Jarin, M.; Zhang, H.; Lai, Y.-C.; He, T.; Kim, H.; Park, I.; Ahn, J.; Huynh, N. D.; Yang, Y.; Wang, Z. L.; Baik, J. M.; Choi, D. Recent Advances in Triboelectric Nanogenerators: From Technological Progress to Commercial Applications. *ACS Nano* **2023**, *17* (12), 11087−11219.

(7) Khanapurarm, U. K.; Rani, G. M.; Panda, S.; Charoonsuk, T.; Mistewicz, K.; Hajra, S.; Kaja, K. R.; Umapathi, R.; Sriphan, S.; Jaļa, J.;

Divi, H.; Smalcerz, A.; Belal, M.; Jaahnavi, P.; Safarkhani, M.; Kim, H.; Mishra, Y. K.; Kim, H. J.; Huh, Y. S.; Vittayakorn, N.; Nowacki, B.; Ravi, S. K.; Eichhorn, S. J.; Craciun, M. F.; Borras, A.; Khanbareh, H.; Qin, J.; Rajaboina, R. K. Harvesting Energy from Friction: The Revolutionary Decade of Triboelectric Nanogenerators. *Adv. Powder Mater.* **2026**, *5*, No. 100373.

(8) Chakraborthy, A.; Prokopchuk, A.; Mamillapalli, G.; H, H.; Langer, E.; Nuthalapati, S.; Nag, A.; Altinsoy, M. E. Smart Glove Integrated Sponge-Based Composite Sensors for Haptic Sensing Applications. *ACS Appl. Electron. Mater.* **2025**, *7* (11), 4822−4831.

(9) Slater, B.; Tan, J.-C. Triboelectric Behaviour of Selected Zeolitic-Imidazolate Frameworks: Exploring Chemical, Morphological and Topological Influences. *Chem. Sci.* **2024**, *15* (26), 10056−10064.

(10) Wang, Y.; Yang, X.; Yu, X.; Duan, J.; Yang, Q.; Duan, Y.; Tang, Q. Triboelectric Charging Behaviors and Photoinduced Enhancement of Alkaline Earth Ions Doped Inorganic Perovskite Triboelectric Nanogenerators. *Nano Energy* **2020**, *77*, No. 105280.

(11) Meng, H.; Yu, Q.; Liu, Z.; Gai, Y.; Xue, J.; Bai, Y.; Qu, X.; Tan, P.; Luo, D.; Huang, W.; Nie, K.; Bai, W.; Hou, Z.; Tang, R.; Xu, H.; Zhang, Y.; Cai, Q.; Yang, X.; Wang, Z. L.; Li, Z. Triboelectric Performances of Biodegradable Polymers. *Matter* **2023**, *6* (12), 4274−4290.

(12) Zhang, R.; Dahlström, C.; Zou, H.; Jonzon, J.; Hummelgård, M.; Örtegren, J.; Blomquist, N.; Yang, Y.; Andersson, H.; Olsen, M.; Norgren, M.; Olin, H.; Wang, Z. L. Cellulose-Based Fully Green Triboelectric Nanogenerators with Output Power Density of 300 W m^{-2}. *Adv. Mater.* **2020**, *32* (38), No. 2002824.

(13) Chen, Q.; Shang, H.; Cheng, B.; Lu, C.; Wang, Y.; Zhang, Y.; Shao, T. Quantifying Triboelectric Series of Polymers Based on the Measurement of Triboelectrification with NaCl Solution. *Chem. Eng. J.* **2024**, *488*, No. 150871.

(14) Zhang, S.; Rana, S. S.; Bhatta, T.; Pradhan, G. B.; Sharma, S.; Song, H.; Jeong, S.; Park, J. Y. 3D Printed Smart Glove with Pyramidal MXene/Ecoflex Composite-Based Toroidal Triboelectric Nanogenerators for Wearable Human-Machine Interaction Applications. *Nano Energy* **2023**, *106*, No. 108110.

(15) Zhang, S.; Sharifuzzamn, M.; Rana, S. M. S.; Zahed, M. A.; Sharma, S.; Shin, Y.; Song, H.; Park, J. Y. Highly Conductive, Stretchable, Durable, Skin-Conformal Dry Electrodes Based on Thermoplastic Elastomer-Embedded 3D Porous Graphene for Multifunctional Wearable Bioelectronics. *Nano Res.* **2023**, *16* (5), 7627−7637.

(16) Ling, Z.; Lin, F.; Huang, X.; Pang, H.; Zhang, Q.; Zhang, C.; Li, X.; Wang, X.; Pan, X. Influence of Molecular Structure and Material Properties on the Output Performance of Liquid−Solid Triboelectric Nanogenerators. *Micromachines* **2023**, *14* (10), No. 1825.

(17) Huang, Y.; Zheng, H.; Zhang, J.; Shen, Y.; Xu, X. Native Proteins for Triboelectric Nanogenerators. *J. Mater. Chem. C* **2025**, *13* (6), 2578−2605.

(18) Rachamalla, A. K.; Navaneeth, M.; Banoo, T.; Deepshikha; Rebaka, V. P.; Kumar, Y.; Rajaboina, R. K.; Nagarajan, S. A High Performance Triboelectric Nanogenerator Using Assembled Sugar Naphthalimides for Self-Powered Electronics and Sensors. *Chem. Eng. J.* **2024**, *490*, No. 151800.

(19) Han, B.-Y.; Pan, T.-Y.; Wu, Y.-C.; Lin, J. T.; Chou, H.-H.; Li, C.-T. Steric Effect of *N* -Substituted Triphenylamine on Double-Anchored Phenothiazine Dye-Sensitized Solar Cells. *ACS Appl. Energy Mater.* **2023**, *6* (7), 3778−3788.

(20) Tong, S.; Zhu, J.; Wang, Z.; Yan, J. Highly Selective SO_2 Capture by Triazine-Functionalized Triphenylamine-Based Nanoporous Organic Polymers. *ACS Appl. Mater. Interfaces* **2024**, *16* (32), 42717−42725.

(21) Zhuang, Y.-C.; Hsiao, S.-H. Visible and Near-Infrared Electrochromic Polyamides and Polyimides Featuring a Phenothiazine-Triphenylamine Star-Shaped Architecture. *ACS Appl. Polym. Mater.* **2025**, *7* (18), 12367−12377.

(22) Ibrahim, M.; Jiang, J.; Wen, Z.; Sun, X. Surface Engineering for Enhanced Triboelectric Nanogenerator. *Nanoenergy Adv.* **2021**, *1* (1), 58−80.

(23) Potu, S.; Navaneeth, M.; Bhadoriya, A.; Bora, A.; Sivalingam, Y.; Babu, A.; Velpula, M.; Gollapelli, B.; Rajaboina, R. K.; Khanapuram, U. K.; Divi, H.; Kodali, P.; Bochu, L. Enhancing Triboelectric Nanogenerator Performance with Metal−Organic-Framework-Modified ZnO Nanosheets for Self-Powered Electronic Devices and Energy Harvesting. *ACS Appl. Nano Mater.* **2023**, *6* (24), 22701−22710.

(24) Cheng, L.; Xu, Q.; Zheng, Y.; Jia, X.; Qin, Y. A Self-Improving Triboelectric Nanogenerator with Improved Charge Density and Increased Charge Accumulation Speed. *Nat. Commun.* **2018**, *9* (1), No. 3773.

(25) Zhang, H.; Hao, Q.; Liu, H. A Flat-Structured Triboelectric Nanogenerator Based on PDMS/MXene for Mechanical Energy Harvesting Boxing Training Monitoring. *AIP Adv.* **2024**, *14* (11), No. 115119, DOI: 10.1063/5.0238763.

(26) Rana, S. M. S.; Wang, Z. L. Recent Advances and Prospective Strategies for Improving the Performance of Triboelectric Nanogenerators. *Coord. Chem. Rev.* **2025**, *543* (34), No. 216914.

(27) Zahed, M. A.; Rana, S. M. S.; Faruk, O.; Islam, M. R.; Reza, M. S.; Lee, Y.; Pradhan, G. B.; Asaduzzaman, M.; Kim, D.; Bhatta, T.; Park, J. Y.; Zahed, M. A.; S Rana, S. M.; Faruk, O.; Islam, M. R.; Reza, M. S.; Lee, Y.; Pradhan, G. B.; Asaduzzaman, M.; Kim, D.; Bhatta, T.; Park, J. Y. Self-Powered Wireless System for Monitoring Sweat Electrolytes in Personalized Healthcare Wearables. *Adv. Funct. Mater.* **2025**, *35* (19), No. 2421021.

(28) Madathil, N.; Potu, S.; Pani, J.; Bochu, L.; Babu, A.; Borkar, H.; Kodali, P.; Khanapuram, U. K.; Rajaboina, R. K. Enhancing Triboelectric Nanogenerators Performance with MXene−Silicone Nanocomposites: A Leap Forward in Energy Harvesting and Touch-Sensitive Technologies. *ACS Appl. Electron. Mater.* **2024**, DOI: 10.1021/acsaelm.4c00503.

(29) Jella, V.; Ippili, S.; Yoon, S.-G. Dielectric Tailoring of Perovskite-Polymer Composites for High-Performance Triboelectric Nanogenerators. *Polymers* **2025**, *17* (7), No. 969.

(30) Yang, S.; Goncharenko, D. V.; Ji, P.; Grozova, N. A.; Semencha, A. V.; Larionova, T. V.; Tolochko, O. V. A Carbon Nanotube-Doped Polyurethane Nanocomposite-Based Triboelectric Nanogenerator: A Platform for Efficient Mechanical Energy Harvesting and Self-Powered Motion Sensing. *ACS Appl. Mater. Interfaces* **2025**, *17* (26), 38469−38480.

(31) Xu, H.; Wang, X.; Niu, J.; Nan, Y.; Pu, J.; Zhou, H.; Duan, J.; Huang, Y.; Hou, B. Construction of MXene/PDMS-Based Triboelectric Nanogenerators for High-Performance Cathodic Protection. *Adv. Mater. Interfaces* **2022**, *9* (11), No. 2102085.

(32) Hasan, M. M.; Ety, N. S.; Islam, F.; Bhowmik, S.; Kamaruzzaman; Rana, S. M. S. Natural Biowaste Material-Based Green Triboelectric Nanogenerators for Self-Powered Gait Monitoring. *RSC Adv.* **2026**, *16* (4), 3281−3295.

(33) Faruk, O.; Islam, M. R.; Rana, S. M. S.; Pradhan, G. B.; Kim, H. S.; Asaduzzaman, M.; Bhatta, T.; Park, J. Y. V2CTX-MXene-Functionalized Fluoropolymer Composite Nanofibrous Mat-Based High-Performance Triboelectric Nanogenerator for Self-Powered Human Activity and Posture Monitoring. *Nano Energy* **2024**, *127* (5), No. 109787.

(34) Thangavelu, H. H. S.; Huang, C.; Chabanais, F.; Palisaitis, J.; Persson, P. O. Å. A Review on MXene Terminations. *Adv. Funct. Mater.* **2026**, *36*, No. e15604.

(35) Deng, S.; Akram, W.; Ye, X.; Zhang, L.; Yang, Y.; Cheng, S.; Fang, J. Comprehensive Insights on MXene-Based TENGs: From Structures, Functions to Applications. *Small* **2024**, *20* (51), No. 2404872.

(36) Ghorbanzadeh, S.; Zhang, W. Advances in MXene-Based Triboelectric Nanogenerators. *Nano Energy* **2024**, *125*, No. 109558.

(37) Subramanyam, S.; Suman; Phor, L.; Chaudhary, V.; Kaushik, V.; Kumar, P.; Chahal, S. Progress in MXene Synthesis Approaches for Energy Systems: A Comprehensive Review. *J. Energy Storage* **2024**, *92*, No. 112043.

(38) Dong, Y.; Mallineni, S. S. K.; Maleski, K.; Behlow, H.; Mochalin, V. N.; Rao, A. M.; Gogotsi, Y.; Podila, R. Metallic MXenes:

A New Family of Materials for Flexible Triboelectric Nanogenerators. *Nano Energy* **2018**, *44*, 103−110.
(39) Wu, H.; Wang, S.; Wang, Z.; Zi, Y. Achieving Ultrahigh Instantaneous Power Density of 10 MW/M2 by Leveraging the Opposite-Charge-Enhanced Transistor-like Triboelectric Nanogenerator (OCT-TENG). *Nat. Commun.* **2021**, *12* (1), No. 5470.
(40) Gao, Y.; Liu, J.; Zhou, L.; He, L.; Liu, D.; Yang, P.; Jin, B.; Wang, Z. L.; Wang, J. Achieving High Performance Triboelectric Nanogenerators Simultaneously with High-Voltage and High-Charge Energy Cycle. *Energy Environ. Sci.* **2024**, *17* (22), 8734−8744.
(41) Liu, J.; Zhou, L.; Gao, Y.; Yang, P.; Liu, D.; Qiao, W.; Zhang, B.; Zhao, Z.; Wang, Z. L.; Wang, J. Achieving Ultra-High Voltage (≈10 KV) Triboelectric Nanogenerators. *Adv. Energy Mater.* **2023**, *13* (21), No. 2300410.
(42) Salauddin, M.; Rana, S. M. S.; Sharifuzzaman, M.; Song, H. S.; Reza, M. S.; Jeong, S. H.; Park, J. Y. Highly Electronegative V2CTx/Silicone Nanocomposite-Based Serpentine Triboelectric Nanogenerator for Wearable Self-Powered Sensors and Sign Language Interpretation. *Adv. Energy Mater.* **2023**, *13* (10), No. 2203812.
(43) Badgurjar, D.; Sudhakar, K.; Jain, K.; Kalantri, V.; Venkatesh, Y.; Duvva, N.; Prasanthkumar, S.; Sharma, A. K.; Bangal, P. R.; Chitta, R.; Giribabu, L. Ultrafast Intramolecular Photoinduced Energy Transfer Events in Benzothiazole−Borondipyrromethene Donor−Acceptor Dyads. *J. Phys. Chem. C* **2016**, *120* (30), 16305−16321.
(44) Chuncha, V.; Balahoju, S. A.; Dutta, S.; Giribabu, L.; Chitta, R. Investigating the Role of Corrole as an Excitation Energy Relay in Light-induced Processes in Closely Connected N,N" -bis(Biphenyl-4-yl)Aniline Functionalized Corrole Donor−Acceptor Dyad. *Photochem. Photobiol.* **2024**, *100* (4), 1041−1054.
(45) Ahlawat, N.; Gupta, M.; Verma, A.; Yadav, B. C. MXene Synthesis Techniques and Their VOCs Sensing Applications. *J. Electrochem. Soc.* **2025**, *172* (4), No. 047507.
(46) Iakunkov, A.; Boulanger, N.; Gurzeda, B.; Li, G.; Hennig, C.; Svitlyk, V.; Jørgensen, M. R. V.; Kantor, I.; Baburin, I. A.; Hamedi, M. M.; Talyzin, A. V. In Situ X-Ray Diffraction Study of MXene Synthesis by the Reaction of Ti_3AlC_2 with Molten Zinc and Tin Chlorides. *Chem. Mater.* **2025**, *37* (3), 1132−1142.
(47) Iqbal, M. A.; Tariq, A.; Zaheer, A.; Gul, S.; Ali, S. I.; Iqbal, M. Z.; Akinwande, D.; Rizwan, S. Ti_3C_2 -MXene/Bismuth Ferrite Nanohybrids for Efficient Degradation of Organic Dyes and Colorless Pollutants. *ACS Omega* **2019**, *4* (24), 20530−20539.
(48) Parker, T.; Zhang, Y.; Shevchuk, K.; Zhang, T.; Khokhar, V.; Kim, Y.-H.; Kadagishvili, G.; Bugallo, D.; Tanwar, M.; Davis, B.; Kim, J.; Fakhraai, Z.; Hu, Y.-J.; Jiang, D.; Talapin, D. V.; Gogotsi, Y. *In Situ* Raman and Fourier Transform Infrared Spectroscopy Studies of MXene−Electrolyte Interfaces. *ACS Nano* **2025**, *19* (24), 22228−22239.
(49) Sarycheva, A.; Gogotsi, Y. Raman Spectroscopy Analysis of the Structure and Surface Chemistry of $Ti_3C_2T_x$ MXene. *Chem. Mater.* **2020**, *32* (8), 3480−3488.
(50) Parker, T.; Zhang, D.; Bugallo, D.; Shevchuk, K.; Downes, M.; Valurouthu, G.; Inman, A.; Chacon, B.; Zhang, T.; Shuck, C. E.; Hu, Y.-J.; Gogotsi, Y. Fourier-Transform Infrared Spectral Library of MXenes. *Chem. Mater.* **2024**, *36* (17), 8437−8446.
(51) Mao, J.; Wen, Y.; Feng, X.; Xu, W.; Seo, S. Multi-Sized Porous Silica/PDMS Composite Layer for Enhanced Performance in Triboelectric Nanogenerators. *Appl. Surf. Sci.* **2025**, *687*, No. 162291.
(52) Choi, G.-J.; Baek, S.-H.; Lee, S.-S.; Khan, F.; Kim, J. H.; Park, I.-K. Performance Enhancement of Triboelectric Nanogenerators Based on Polyvinylidene Fluoride/Graphene Quantum Dot Composite Nanofibers. *J. Alloys Compd.* **2019**, *797*, 945−951.
(53) Shi, L.; Jin, H.; Dong, S.; Huang, S.; Kuang, H.; Xu, H.; Chen, J.; Xuan, W.; Zhang, S.; Li, S.; Wang, X.; Luo, J. High-Performance Triboelectric Nanogenerator Based on Electrospun PVDF-Graphene Nanosheet Composite Nanofibers for Energy Harvesting. *Nano Energy* **2021**, *80*, No. 105599.
(54) Li, S.; Hu, Y.; He, P.; Qu, J.; Zhao, J.; Mo, J.; Fan, Z. Enhanced Performance of TENG through Graphene Oxide and Transition Layer Coupling: Achieving Green Energy Harvesting and Powering Wearable Devices. *Nano Energy* **2025**, *133*, No. 110436.
(55) Kavarthapu, V. S.; Paranjape, M. V.; Manchi, P.; Kurakula, A.; Lee, J. K.; Graham, S. A.; Yu, J. S. Wireless Alerts and Data Monitoring from BNNO-MWCNTs/PDMS Composite Film-Based TENG Integrated Inhaler for Smart Healthcare Application. *Small* **2024**, *20* (44), No. 2403218.
(56) Zhang, J.; Boyer, C.; Zhang, Y. X. Enhancing the Humidity Resistance of Triboelectric Nanogenerators: A Review. *Small* **2024**, *20* (36), No. 2401846.
(57) Somkuwar, V. U.; Garg, H.; Maurya, S. K.; Kumar, B. Influence of Relative Humidity and Temperature on the Performance of Knitted Textile Triboelectric Nanogenerator. *ACS Appl. Electron. Mater.* **2024**, *6* (2), 931−939.

https://doi.org/10.1021/acsaelm.5c02701
ACS Appl. Electron. Mater. XXXX, XXX, XXX−XXX